NUMERICAL ANALYSIS OF THE DEPENDENCY OF THE WELD POOL SHAPE ON TURBULENCE AND THERMODYNAMIC ACTIVITY OF SOLUTES IN LASER BEAM WELDING OF UNALLOYED STEELS

A. ARTINOV*, P. KISING*, M. BACHMANN*, X. MENG*, M. RETHMEIER**,*,***

**Bundesanstalt für Materialforschung und -prüfung (BAM), Unter den Eichen 87, 12205 Berlin, Germany*
***Institute of Machine Tools and Factory Management, Technische Universität Berlin, Pascalstraße 8-9, 10587 Berlin, Germany*
****Fraunhofer Institute for Production Systems and Design Technology, Pascalstraße 8-9, 10587 Berlin, Germany*

DOI 10.3217/978-3-85125-968-1-09

ABSTRACT

A three-dimensional numerical model was developed to accurately predict the steady-state weld pool shape in full penetration laser beam welding. The model accounts for the coupling between the heat transfer and the fluid dynamics by considering the effects of solid/liquid phase transition, thermo-capillary convection, natural convection, and phase-specific and temperature-dependent material properties up to the evaporation temperature. A fixed right circular cone was utilized as a keyhole geometry to consider the heat absorbed from the laser beam. The model was used to analyze the influence of the thermodynamic activity of solutes and turbulence on the weld pool shape. A mesh sensitivity analysis was performed on a hybrid mesh combining hexahedral and tetrahedral elements. For the case of full penetration laser beam welding of 8 mm thick unalloyed steel sheets, the dependence of the weld pool shape on the surface-active element sulfur was found to be negligible. The analysis of the results showed that a laminar formulation is sufficient for accurately predicting the weld pool shape since the turbulence has a minor impact on the flow dynamics in the weld pool. The validity of the numerical results was backed up by experimental measurements and observations, including weld pool length, local temperature history, and a range of metallographic cross-sections.

Keywords: Weld pool shape, Numerical modeling, Laser beam welding, Thermo-capillary convection, Turbulence

INTRODUCTION

In recent years, due to the increase in available power outputs of solid-state lasers, modern laser systems allow joining parts in the thickness range of up to 50 mm by single-pass welding [1, 2]. Furthermore, the laser beam welding process brings various advantages, e.g., a narrow heat-affected zone, high efficiency and reproducibility of the welds, high reachable penetration depths and welding speeds, as well as high adaptability of the process. Therefore, the number of applications of the laser beam welding process rises steadily, not only in the workshop but also in the fields [3], e.g., in shipbuilding, by the production of pipelines, high-pressure and vacuum vessels, etc.

Nonetheless, as research results in the past have shown, various defects occur with the increase in welding speed and sheet thickness. These defects include hot cracking [4-7], porosity, laser keyhole instability and collapse [8-9], and other defects.

The formation of these defects is long known to be due to the underlying physical phenomena governing the weld pool dynamics [10]. Studies on laser arc hybrid welding showed that there is a correlation between the weld pool characteristics and the amount of residual porosity in the final weld [11]. The authors examined this correlation under different welding parameters and introduced a characteristic coefficient to predict the amount of residual porosity in the final weld. Multiple studies on the formation of hot cracking showed that there is a strong coherence between the weld pool geometry and the formation of cracks, especially in the so-called bulging region [12-14]. In [15], the relationship between the bulging region and the hot cracking formation in deep penetration laser beam welding was studied, and the authors concluded that the formation of a bulging region in the weld pool directly increases the hot cracking susceptibility.

Due to the importance of the weld pool geometry on the occurring defects and the increase of quality requirements in terms of reproducibility and parameter optimization in modern industry, it is crucial to get further insights into the laser beam welding process. Since extensive experiments and parameter studies are both time-consuming and cost-intensive, it is necessary to develop mathematical models to simulate the laser beam welding process. Nowadays, computational units have the capacity to simulate even very complex physical phenomena. Nevertheless, this has not always been the case, as in the early stages of modeling, researchers did not have the computational power to account for the fluid flow and mass transfer. Moreover, in terms of heat sources, simple point, line, and volumetric heat sources are not sufficient for an accurate description of the energy distributed on the keyhole surface [16-17]. In later stages, when the fluid flow was modeled as well, the accuracy of the results greatly improved. In the beginning, such models were primarily two-dimensional [17-19], until eventually in the 80s the three-dimensional weld pool flow was studied [20]. From there on, with increasing computational power and understanding of the laser beam welding process, the development of thermo-fluid dynamics models, allowing to fully couple the fluid flow and the heat transfer, followed.

In the present time, thermo-fluid dynamics models can be separated into two groups, models that contain a predefined keyhole geometry which is part of the computational domain, aiming to find a balance between simulation time and numerical accuracy, e.g. [21], and dynamic keyhole models that aim to simulate the laser welding process very precisely, e.g. [22-26]. Nevertheless, the development of dynamic models is a very time-

consuming, computer-intensive, and challenging procedure. These models are usually calculated as transient, thus having high runtimes, while only predicting one to two seconds of the actual laser beam welding process. Therefore, simplified models, based on empirical approximations of physical phenomena are highly important for case and parametric studies or more practical applications. In addition, works in the past have shown that models with strong physical simplifications are able to predict the weld pool geometry and fluid flow well even though under short computation times, e.g. [27]. Although many researchers worked with simplified models in the past, there are still various factors that are not sufficiently investigated yet. Turbulence is considered in some works, e.g. [21, 27], but disregarded in most other works. Furthermore, when turbulence is accounted for, primarily the well-known k-ε model is utilized, however, there is no validation that this turbulence model is the most suitable to predict the weld pool geometry. The same tendency is observed for the modeling of the thermo-capillary convection, from now on referred to as the Marangoni convection in the present paper. To the best of the authors' knowledge, in most of the published works on the topic the simplified implementation of the Marangoni convection is utilized, i.e., it is considered without accounting for the influence of the surface-active elements, e.g. [21, 27]. Even though these works obtained reasonable results, it is uncertain how the inclusion of surface-active elements influences the weld pool geometry, especially when unalloyed and low-alloyed steels, which typically contain a very low amount of surface-active elements, are studied. In addition, there are few studies on mesh sensitivity showing that the numerically obtained solution is mesh independent, i.e., the solution does not change when reducing the element size.

The present work seeks to investigate the dependency of the weld pool shape on turbulence and thermodynamic activity of solutes in laser beam welding of unalloyed steels and to validate the numerical results by comparing them to experimentally obtained results. Moreover, a mesh sensitivity study is performed to investigate the required minimum element size to account for an adequate numerical accuracy for the case under consideration.

METHODOLOGY

MATERIALS

In the welding experiments the unalloyed structural steel EH36-N was utilized. The dimensions of the sheets were 300 mm x 100 mm x 8 mm. The chemical composition was obtained by spectral analysis; the corresponding values in wt.% are listed in Tab. 1. As seen from Table1, the chemical composition of the material is comparable with this of the structural steel S355 according to the corresponding standard, see DIN EN 10025-2 [28]. Note that the amount of sulfur in the EH36-N steel sheets is very low and therefore the maximum values were taken from the standard and not from the measurement.

Table 1 Chemical composition of the unalloyed steel EH36-N in wt.%; top: standard DIN EN 10025, bottom: experimental measurements with spectral analysis

C	Si	Mn	Al	Nb	Ni	Cu	Cr	P	S	V	Fe
≤0.2	≤0.55	≤1.6	-	-	-	≤0.55	-	≤0.025	≤0.035	-	bal.

C	Si	Mn	Al	Nb	Ni	Cu	Cr	P	S	V	Fe
0.132	0.260	1.400	0.028	0.036	0.040	0.012	0.040	0.025	0.035	0.006	bal.

EXPERIMENTS

The processing parameters are summarized in Table 2. Thermocouples of type K with a diameter of 0.25 mm were placed in the middle of the sheet at a lateral distance of around 1 mm from the weld centerline. The positions of the thermocouples on the bottom side were nearly identical to those on the upper side of the workpiece. The exact positions were measured after the welding process with an optical microscope. A schematic showing the starting and ending positions of the laser and the locations of the thermocouples is given in Fig. 1. The complete experimental setup is shown in Fig. 2. Thereby, a diode laser and a high-speed camera were used to illuminate the weld pool on the top surface and measure the weld pool length, respectively.

Table 2 Processing parameters of the experiments

Parameters	Value	SI-Unit
Laser type	Yb:YAG disc laser	–
Wavelength	1030	nm
Laser power P_{L}	8	kW
Focal diameter	500	µm
Focal length	300	mm
Focal position	0	mm
Laser torch angle	0	deg
Shielding gas	M21	–
Gas flow rate	25	$\mathrm{L\ min^{-1}}$
Welding speed u_{weld}	2	$\mathrm{m\ min^{-1}}$

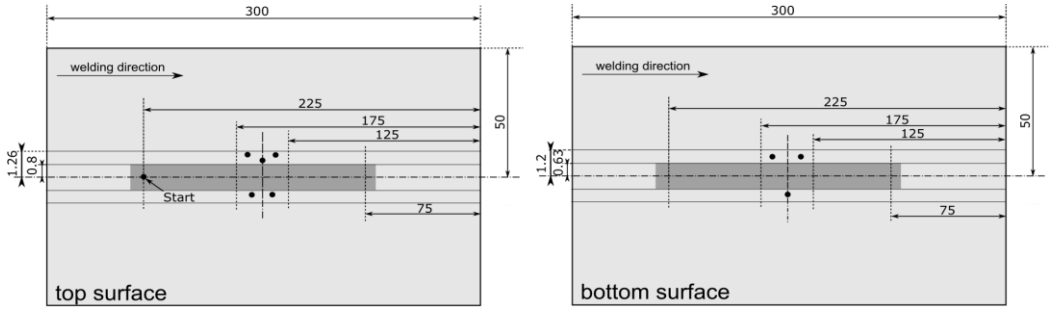

Fig. 1 Experimental setup of the temperature measurements. The thermocouples are highlighted by the black dots.

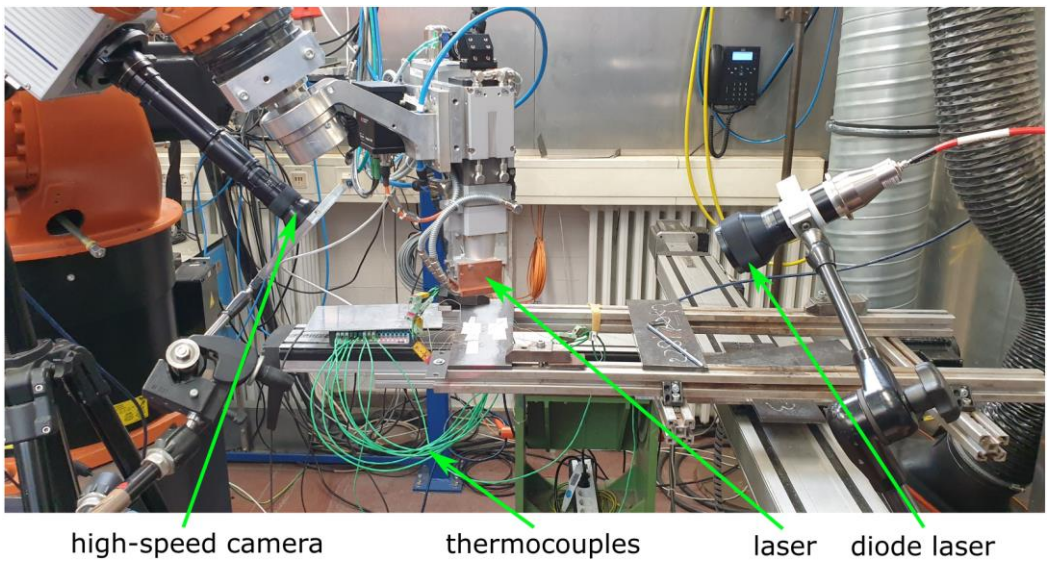

Fig. 2 Experimental setup

NUMERICAL MODELING

A three-dimensional numerical model was developed to accurately predict the steady-state weld pool shape in full penetration laser beam welding. The model is based on several previous works with optimizations regarding the prediction of the weld pool shape as well as the weld pool flow. Further information can be obtained from [20, 21, 27].

Assumptions

The basic assumptions for thermo-fluid dynamics simulation are according to [21, 27]. These are given as follows:

- Since the process is continuous and the sheets are welded on a linear trajectory, a quasi-steady-state approach was used to mathematically describe the weld pool shape and the local temperature field. Thus, temporal oscillations of the weld pool or the keyhole surfaces were neglected, and the start and the end of the welding process were not modeled.
- The size of the computational domain for the stationary thermo-fluid dynamics simulation was adapted to justify the usage of an adiabatic boundary condition defined on the rear surface, see Fig. 3.
- Fixed geometry of the top and bottom surfaces as well as of the keyhole surface were used, i.e., the recoil pressure was assumed to be perfectly balanced by the surface tension force on the keyhole surface. Furthermore, these surfaces were assumed to be frictionless, and an inclination of the keyhole geometry was not considered due to the comparatively low welding speed used in the experiments, see Tab. 2. The fixed geometry of the keyhole was further exploited as an equivalent heat source (EHS), i.e., the surface temperature of the keyhole was prescribed by the evaporation temperature of the material. This EHS technique assumes that the temperature in the keyhole should be at least equal or higher than the evaporation temperature of the material since part of the material on the keyhole surface vaporizes [29]. Thereby, the keyhole radii can be used as calibration parameter for the EHS. Note, however, that the radii used in the model should lie in the range of the focal spot radius of 250 μm. In the present work the top radius was chosen to be 0.31 mm and the bottom radius was set 0.19 mm.
- In the first simulation stage a laminar formulation was used to predict the weld pool shape. This approach is reasonable, as the areas where high velocities and thus high Reynolds numbers appear are limited to the usually small surface areas that are influenced by the Marangoni convection. In the second simulation stage, three different turbulence models were utilized, including the SST k-ω model, the SST γ transition model, and the SST γ-Re_{Θ} transition model.
- The Boussinesq approximation was used to model the impact of the density deviation, caused by the temperature difference, on the fluid flow in the weld pool [30].
- Solidification was modeled by the enthalpy-porosity approach [31], using the Carman-Kozeny equation for porous media morphology.
- The material properties were taken from the literature and modeled as temperature-dependent up to the evaporation temperature [32–36].
- Heating by the laser induced metal vapor was not considered due to the small differences between the evaporation temperature of the material and the metal vapor temperature as well as the low heat absorption for the wavelength of around 1 μm [37-39].

- Heat losses by radiation were not accounted for due to the high relation of volume versus surface of the steel sheet, e.g. [40].
- The shear stress due to the interaction of evaporating material on the liquid metal was neglected as there is no experimental validation of the velocity distribution along the keyhole surface. Moreover, there is a high discrepancy in the numerically predicted magnitudes of the vapor velocities, e.g. [29, 41-43].
- Since the heat transport at the surface is mainly driven by the Marangoni convection via convective energy transport, the heat exchange with the environment is considered negligible.

Governing equations

The governing equations for the conservation of mass, momentum, and energy are given in the following in the form as these are implemented in the finite volume software ANSYS Fluent which was used for the computations:

- Mass conservation for incompressible flow

$$\nabla \cdot \mathrm{u} = 0, \tag{1}$$

where $u = (u, v, w)$ is the fluid velocity vector.

- Momentum conservation

$$\nabla \cdot (\rho \mathrm{uu}) = -\nabla p + \nabla \cdot (\mu[\nabla \mathrm{u} + \nabla \mathrm{u}^{\mathrm{T}}]) + \rho \mathrm{g} + \mathrm{F}, \tag{2}$$

with source term *F* given as follows:

$$\mathrm{F} = \mathrm{F}_{\mathrm{buo}} + \tau_{\mathrm{Ma}} + \mathrm{C}_{\mathrm{ck}}. \tag{3}$$

The first term on the right-hand side (RHS), $\mathrm{F}_{\mathrm{buo}}$, uses the Boussinesq approximation to account for the buoyancy force caused by the deviation of the density with temperature:

$$\mathrm{F}_{\mathrm{buo}} = -\rho \mathrm{g} \beta (T - T_{melt}). \tag{4}$$

Here *p, μ,* g and β are the fluid pressure, the dynamic viscosity, the gravity acceleration vector, and the linear volumetric coefficient of thermal expansion, respectively. The second term on the RHS of Eq. 3 accounts for the Marangoni convection, given as:

$$\tau_{\mathrm{Ma}} = -\frac{\partial \gamma}{\partial T} \nabla_{\mathrm{s}} T, \tag{5}$$

where $\nabla_s T$ is the temperature gradient on the surface and $\frac{d\gamma}{dT}$ is the surface tension gradient with respect to temperature [35] which is expressed as:

$$\frac{d\gamma}{dT} = \frac{\partial \gamma}{\partial T} - R\Gamma_s \ln[1 + k_e \alpha] - \frac{k_e \alpha \Delta H^0 \Gamma_s}{T(1 + k_e \alpha)}. \tag{6}$$

In Eq. 6, T is the temperature, R is the universal gas constant, $\frac{\partial \gamma}{\partial T}$ is the Marangoni coefficient, Γ_s is the interface concentration at the melting temperature, k_e is a constant related to the entropy of the phase separation and ΔH^0 is the adsorption heat.

Solidification was modeled with the third term on the RHS of Eq. 3 representing the Carman-Kozeny approach for porous media morphology:

$$\mathrm{C_{ck}} = A_{mush}\frac{(1-f_L)2}{f_L^3+\mathrm{c_1}}(\mathrm{u}-\mathrm{u_{weld}})\,. \tag{7}$$

The parameter A_{mush} is used to adjust the flow damping and is set to 10^6 in the model. The parameter c_1 is set to a very small value to avoid division by zero [44]. In addition, solidification is also modeled with the modified viscosity method [45]:

$$\eta_{eff} = \begin{cases} \eta + f & \text{for } T < T_{sol} \\ \eta + f\left(1 - \frac{T-T_{sol}}{T_{liq}-T_{sol}}\right) & \text{for } T_{sol} \le T \le T_{liq}, \\ \eta & \text{for } T > T_{liq} \end{cases} \tag{8}$$

where η_{eff} is the effective viscosity, η the dynamic viscosity, T_{sol} the solidus temperature, T_{liq} the liquidus temperature, and f a constant that is set to 1 in the current study.

- Energy conservation

$$\nabla\cdot(\rho\mathrm{uH}) = \nabla\cdot(\lambda\nabla\mathrm{T}). \tag{9}$$

Here, λ is the thermal conductivity [46]; the latent heat, ΔH, is defined as:

$$\Delta H = f_L H_f, \tag{10}$$

where the function f_L represents the fraction of the liquid phase and is defined as follows:

$$f_L = \begin{cases} 0 & \text{for } T < T_{sol} \\ \frac{T-T_{sol}}{T_{liq}-T_{sol}} & \text{for } T_{sol} \le T \le T_{liq}. \\ 1 & \text{for } T > T_{liq} \end{cases} \tag{11}$$

The iteration between the energy equation (9) and the liquid fraction equation (11) provides the solution for the temperature [46]. In the case of a turbulent flow pattern, the turbulent transport variables are modeled according to the Carman-Kozeny approach:

$$C_{ck,turb} = A_{mush}\frac{(1-f_L)^2}{f_L^3+c_1}\Phi, \tag{12}$$

where Φ represents the turbulent transport variables in each turbulent case (k, ε, ω etc.) [46].

Boundary conditions

The boundary conditions used in the thermo-fluid dynamics model are presented in Fig. 3 and summarized as follows:

- At the inlet of the computational domain, the temperature is set to the room temperature, while the velocity equals the process velocity $\mathbf{u}_{\mathbf{weld}}$.
- The top, bottom and rear surface, the keyhole surface, and the symmetry plane were set as a free slip condition. Flow components in the normal direction are not present, i.e., $u_n = 0$ applies, and there is no existence of a boundary layer formation at these surfaces.
- The fixed keyhole surface was set to the evaporation temperature of the material.

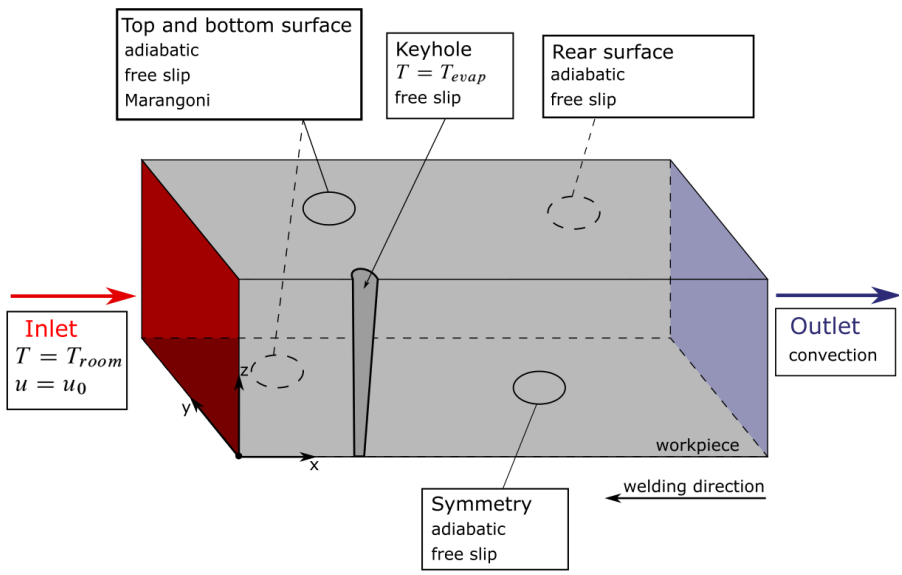

Fig. 3 Boundary conditions for the CFD-simulation

- Since the temperature-dependent Marangoni convection is the main driving force in the weld pool, it was modeled as shear stress on the top and bottom surfaces of the workpiece, expressed as follows:

$$\eta \frac{\partial u}{\partial z} = \frac{\partial \gamma}{\partial T}\frac{\partial T}{\partial x}, \eta \frac{\partial v}{\partial z} = \frac{\partial \gamma}{\partial T}\frac{\partial T}{\partial y}. \tag{13}$$

- The top, bottom and rear surfaces were modeled as adiabatic:

$$\frac{\partial T}{\partial n} = 0. \tag{14}$$

The discretization of the computational domain is, based on an approach that combines tetrahedral and hexahedral elements in a hybrid mesh shown in Fig. 4. While hexahedral elements usually provide good convergence behavior, tetrahedral elements are good at

filling complex geometries. The advantage of combining both types of elements is to resolve the area around the weld pool by using a very fine mesh, while a coarser mesh may be applied at areas outside of the weld pool. This results in an overall smaller number of elements and thus decreases the simulation time. Furthermore, the use of structured elements leads to an easier comparison between different mesh sizes. The inner, white-bordered block in Fig. 4 is very finely meshed, and the used hexahedral nodes are small enough to resolve the physical phenomena well. The transition area between the white and the dashed black lines, was meshed with tetrahedral elements; these gradually become coarser, being finest at the white border and coarser when reaching the dashed black border. The area outside the dashed black border up to the completely black border represents the coarsest meshed area. Note that on the top and the bottom surface of the inner block a prismatic layer was applied. This was chosen so that the velocity gradients caused by the Marangoni convection can be well resolved, thus supporting convergence of the solution.

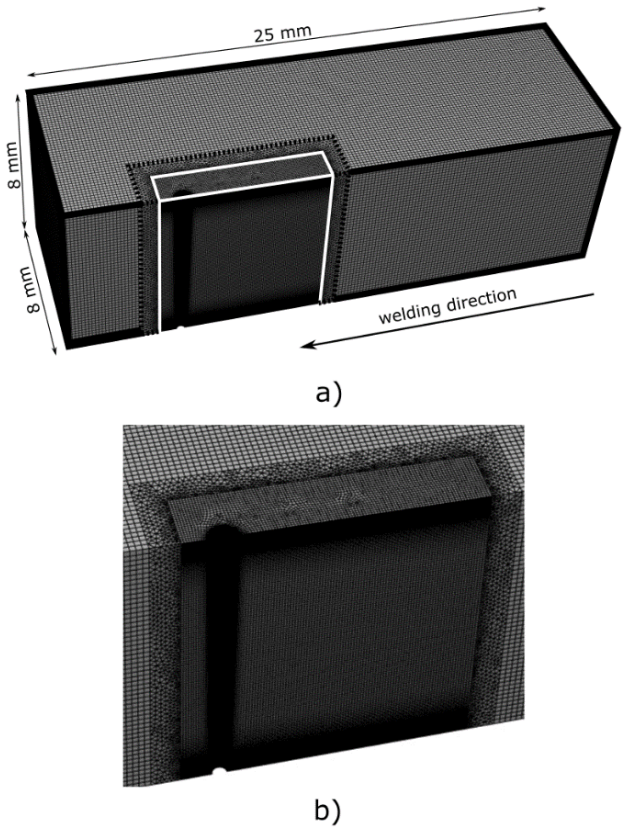

Fig. 4 a) An overview of the computational domain, b) shows an enlarged view of the mesh in the vicinity of the keyhole

In addition, the influence of the Marangoni convection on the formation of the weld pool was studied. Specifically, the Marangoni convection can be implemented

numerically in two different forms, either by neglecting the surface-active elements or considering these. The Marangoni convection describes the resulting shear stresses, which form on the surface of the molten metal due to the temperature dependence of the surface tension. Since the velocities caused by the Marangoni convection can reach very high values, due to the high temperature gradients, a flow is developed within the weld pool, which can be directly attributed to the Marangoni convection. This flow has a strong impact, both on the shape of the weld pool and the transfer of the heat in the vicinity of the weld pool surface. The surface tension gradient can be represented as a function of the temperature and the chemical activity of surface-active elements as seen in Eq. 6 [47]. It can have both, positive and negative values and has a significant influence on the surface flow; thereby in case of a negative coefficient, the melt flows from areas of higher temperature to areas of lower temperature [10]. The first implementation method would be to neglect the surface-active elements (α = 0), thus assuming a constant Marangoni coefficient. The result for a negative constant, which is typical for pure iron, is a flow that is directed away from the hot keyhole surface to the outer edge of the weld pool. However, if the surface-active elements are considered, the flow would instead consist of two opposite-faced vortices [48]. Since the Marangoni convection has a major influence on the formation of the weld pool, a different approach may lead to a significant change in the flow field of the weld pool and thus also on the weld pool geometry.

For the turbulence study, three turbulence models were used to compare the weld pool geometry and the fluid flow therein; these include the SST k-ω model, the γ transition model, and the γ-Re_Θ transition model. An advantage of the transition models is that these can consider both, a laminar and a turbulent flow pattern, in different regions of the weld pool, simultaneously. It is reasonable to apply these models, since the weld pool flow is unlikely to be either completely laminar or turbulent [49]. Because of the vortices that are present when using the variable surface tension gradient, an adverse pressure gradient develops in the region where these collide. Therefore, it is reasonable to assume that the k-ε turbulence model is not the best choice, as it is known to lead to difficulties when an adverse pressure gradient is present [50]. On the other hand, the SST k-ω model represents a good alternative. The turbulence parameters for the different models are the standard values set by Fluent according to empirical measurements and available literature.

Material properties

The material properties are defined as a function of temperature up to the maximum temperature of 3100 K and are shown in Fig. 5, Fig. 6, and Table 3. The value for the steel density was averaged over the interval of interest, between 1200 K and 2800 K, resulting in ρ_{steel} = 7060 kg m^{-3}.

Table 3 Material properties of the unalloyed steel EH36-N

Material property		Value	SI-Unit
Melting temperature	T_{melt}	1750	K
Solidus temperature	T_{sol}	1710	K
Liquidus temperature	T_{liq}	1790	K
Latent Heat	H_f	247000	J kg^{-1}
Thermal expansion	β	$1.5 \cdot 10^{-5}$	K^{-1}
Marangoni coefficient	$\frac{\partial \gamma}{\partial T}$	$-4.3 \cdot 10^{-4}$	N m^{-1} K^{-1}
Surface excess at saturation	Γ_s	$1.3 \cdot 10^{-5}$	mol m^{-2}
Universal gas constant	R	$8.314 \cdot 10^{-3}$	J mol^{-1} K^{-1}
Constant related to the entropy of segregation	k_e	$3.18 \cdot 10^{-3}$	-
Standard heat of adsorption	ΔH^0	$-1.66 \cdot 10^5$	J mol^{-1}
Thermodynamic activity	α	0.035	-

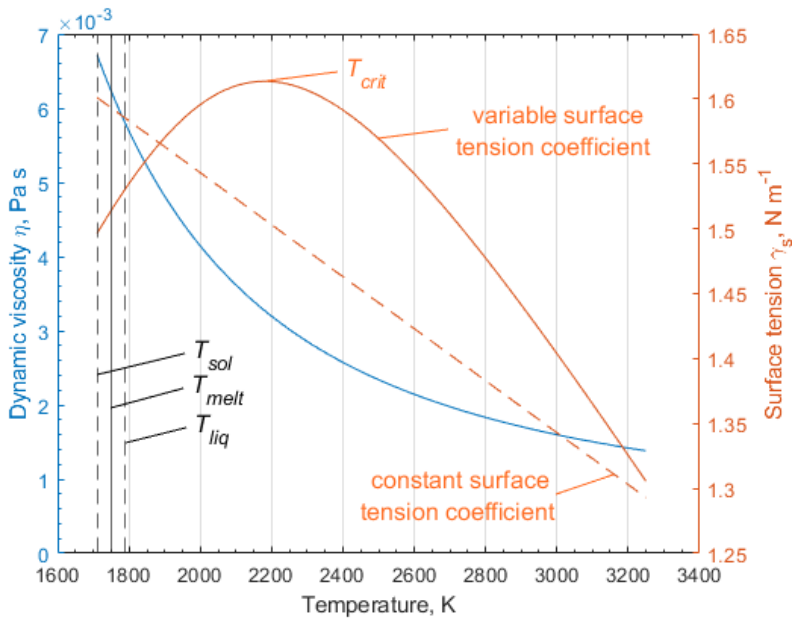

Fig. 5 Thermophysical properties of the unalloyed steel EH36-N

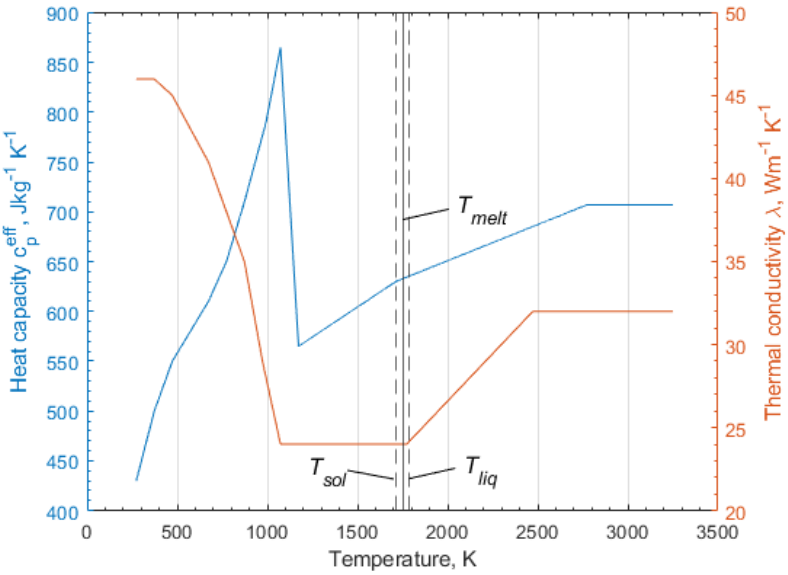

Fig. 6 Thermophysical properties of the unalloyed steel EH36-N

Numerical setup

The modeling framework presented in this work was executed with the finite volume software ANSYS Fluent. For the performed simulations the stationary, pressure-dependent, coupled PISO solver was used. It solves a coupled system of equations consisting of the conservation of momentum and the pressure-based conversation of mass. Calculation of the gradients was performed with the GREEN-GAUSS Node-Based scheme; this approach is more precise compared to the alternative schemes, the Least Squares Cell-Based scheme, and the GREEN-GAUSS Cell-Based scheme, while being heavier in computation work [46]. For the interpolation of the pressure the PRESTO! (PREssure Staggering Option) scheme was used as it led to a good convergence behavior in the simulations. The interpolation for the conservation of momentum was performed with First-Order Upwind scheme; for the energy equation the Second-Order Upwind scheme was used. The difference between the two interpolation types is that the Second-Order Upwind scheme is more precise, but usually leads to a worse convergence behavior, see [46]. In the simulations including a turbulent model, the additional transport parameters were as well interpolated using the First-Order Upwind scheme.

RESULTS

MESH SENSITIVITY STUDY

To account for a mesh-independent solution, a mesh sensitivity study with four different meshes was conducted. Note that only the element size in the inner, white highlighted block in Fig. 4, was changed, since the weld pool is located in this area. Furthermore, all numerically determined weld pool geometries were calculated with a laminar formulation of the flow pattern in the weld pool. The usage of tetrahedral elements in the transition layer also leads to a change in the number of elements in the transition area, since it is directly linked to the elements of the inner block. The specified mesh size of the inner block and the total number of elements for each mesh are summarized in Table 4. An overview of the computed weld pools for the different meshes is shown in Fig. 7. It can be seen that the size of the weld pool computed with mesh 1 is underestimated on the top and bottom sides of the workpiece compared to the solutions obtained with the finer meshes 3 and 4. Compared to mesh 2, the length of the weld pool on the top surface resembles that of mesh 3 and 4, while the length on the bottom surface deviates. The numerical results were considered to be mesh independent for mesh 3, as the weld pool geometry did not change when the finest mesh, mesh 4, was used, see Fig. 8. Therefore, mesh 3 was chosen to be utilized in the present studies, representing the best compromise between numerical accuracy and computational intensity.

Table 4 Meshes and corresponding mesh sizes used for the mesh sensitivity study

Mesh name	Element size in the inner block	Total number of elements	Runtime
Mesh 1	$1 \cdot 10^{-4}$ m	$0.94 \cdot 10^{6}$	20 min
Mesh 2	$8 \cdot 10^{-5}$ m	$1.20 \cdot 10^{6}$	34 min
Mesh 3	$7 \cdot 10^{-5}$ m	$1.42 \cdot 10^{6}$	52 min
Mesh 4	$5 \cdot 10^{-5}$ m	$2.41 \cdot 10^{6}$	91 min

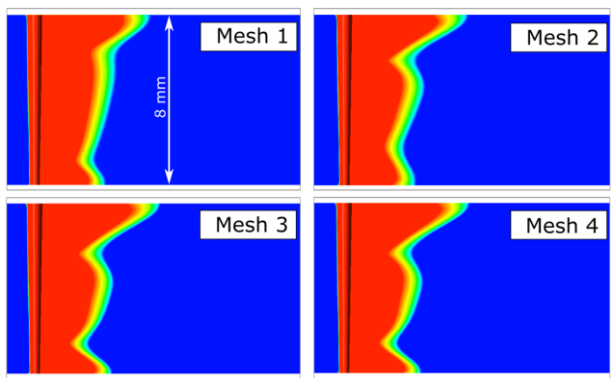

Fig. 7 Numerically determined weld pool geometries in the symmetry plane of the model

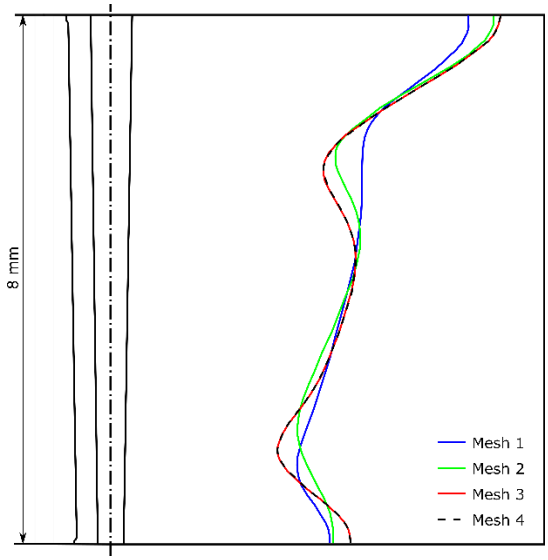

Fig. 8 Comparison of the contours of the weld pools by using the melting isotherms at T_{melt} = 1750 K

EXPERIMENTS

Several cross-sections along the weld seam were obtained to account for the experimental tolerances and to validate the numerically obtained results according to the ISO/TS 18166 standard [51]. Two cross sections, namely the widest and narrowest, were compared to the numerically obtained cross-section. A metallographic specimen is shown in Fig. 9 a), where the fusion line is highlighted in white; in Fig. 9 b) a comparison of all fusion lines was performed; the modeled fusion line is highlighted in black. This was obtained by a projection of the weld pool using the melt temperature T_{melt}. The numerically obtained fusion line agrees well with the two experimentally determined fusion lines. Note that due to the conical approximation of the keyhole geometry in the model, there is a linear decrease in width of the modeled fusion line along the thickness of the steel sheet.

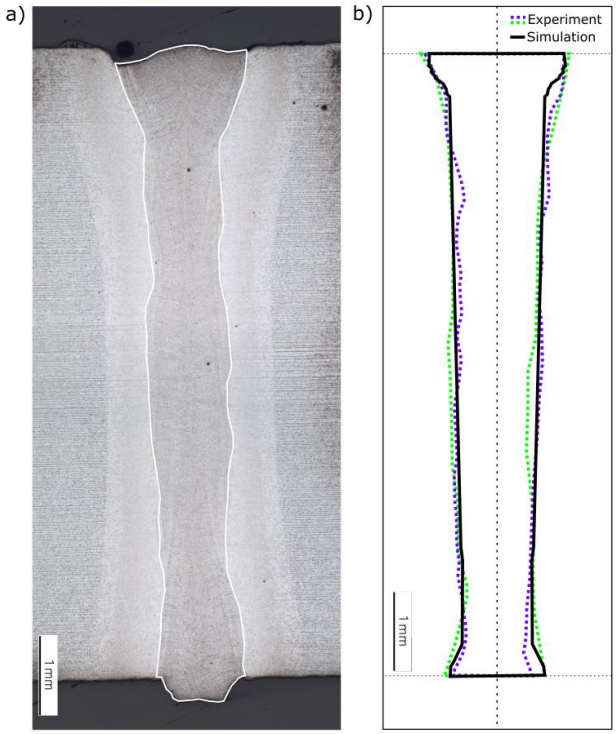

Fig. 9 a) shows an exemplary metallographic cross section from the experiment, b) shows the comparison of the experimentally obtained and numerically predicted fusion lines

In addition, the experimentally determined weld pool length is compared with the modeled weld pool length. In Fig. 10 a) the weld pool on the top surface was recorded by a high-speed camera. As seen in Fig. 10 a), the length of the weld pool has been estimated to approx. 6.3 mm. The experimentally determined weld pool length has been compared with the weld pool length in the model, defined by the fusion isotherm at T_{melt} = 1750 K on the symmetry plane, see Fig. 10 b). As seen, the numerical value of 6.2 mm corresponds very well to the measured one in the experiment.

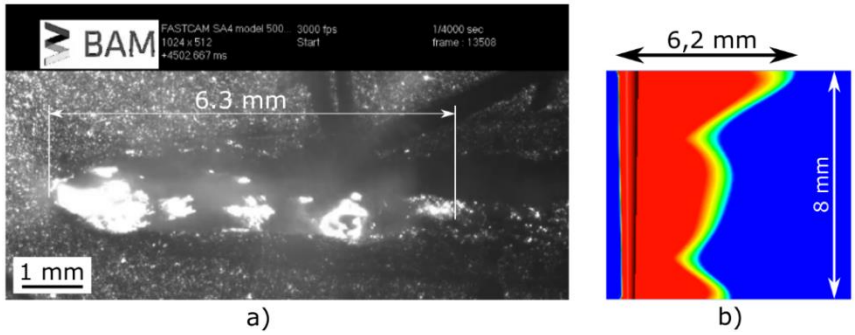

Fig. 10 a) shows the weld pool on the top surface of the steel sheet, recorded by a high speed-camera, b) shows the numerically predicted weld pool for the laminar case

Fig. 11 shows the experimental and numerical time-temperature curves for different distances from the weld centerline. The curves were aligned so that the maximum temperature values measured in the experiment and predicted in the simulation lie on top of each other. As seen from the comparison, the peak temperatures in the experiment as well as in the model are in close agreement. Hence, it can be concluded that the numerical model represents the thermal behavior of the welded steel sheets accurately.

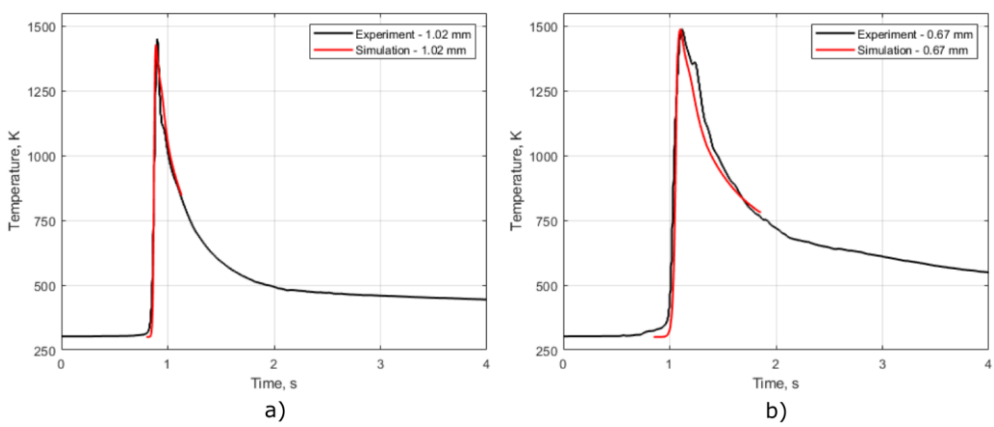

Fig. 11 Comparison of the numerically and experimentally obtained temperature curves a) on the top side of the sheet, b) on the bottom side of the sheet

IMPACT OF THE SURFACE-ACTIVE ELEMENTS ON THE WELD POOL GEOMETRY

The Marangoni convection plays a crucial role on the weld pool geometry and the heat transfer near the surface, usually this is considered as independent of the surface-activity. In the current study, two implementations were considered, neglecting, and considering the surface-active element sulfur. To compare both implementations and derive the best practices concerning their usage, the weld pool geometry was compared in Fig. 12. Note

that when neglecting the surface-active elements, the surface-tension gradient γ'_s was set to -0.00043 N m^{-1} K.

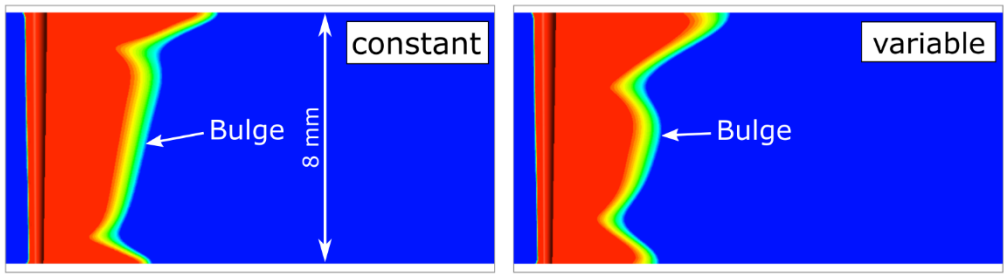

Fig. 12 Comparison of the calculated weld pool geometries in the symmetry plane for the different implementations of the Marangoni convection

It can be seen that the bulge for the variable surface tension gradient is more pronounced because the weld pool is more constricted in the top and bottom part; this can be explained by looking at the strong differences in the fluid flow, seen in Fig. 13. There the black lines highlight the melting isotherms. In the case of a constant surface tension gradient the backflow to the keyhole from the inner weld pool region is located much closer to the top surface.

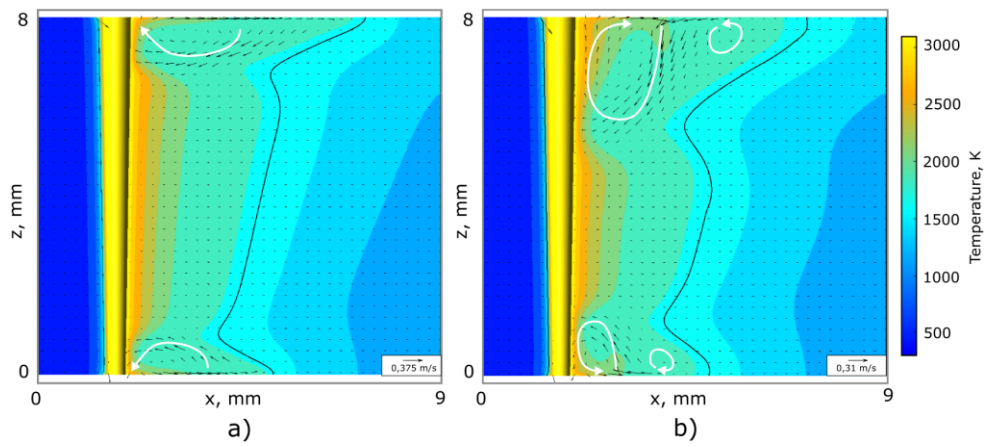

Fig. 13 Comparison of the weld pool flow in the symmetry plane for the different implementations of the Marangoni convection a) constant surface-tension gradient, b) variable surface-tension gradient

This phenomenon can be explained by examining the velocity fields on the top surface shown in Fig. 14. Due to the Marangoni stresses acting in both directions, opposite to the welding direction in the high-temperature region near the keyhole, and in the welding direction near the outer edge of the weld pool, two opposite-faced vortices are formed, which are the cause for the deep backflow.

In Fig. 15 the numerically obtained fusion lines for both approaches are compared to the experimentally obtained fusion lines, showing only minor deviations. In Fig. 16, on the other hand, the melting isotherms for the variable and constant surface tension are compared. These show strong differences in the upper weld pool region and smaller deviations in the lower weld pool region. Based on the results it can be concluded that sulfur amounts of about 350 ppm may lead to visible changes of the shape of the weld pool. However, the total size and especially the length on the top and bottom surfaces remain unchanged.

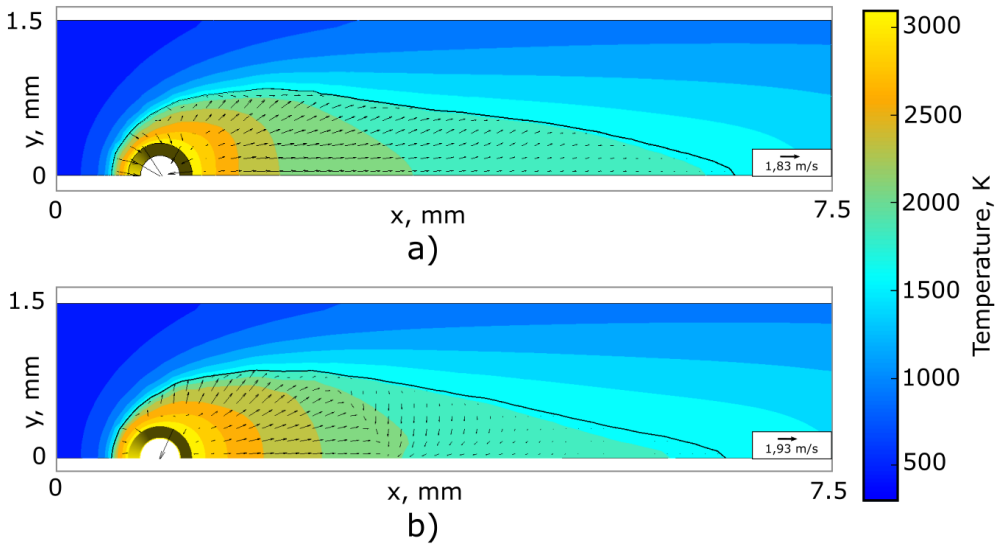

Fig. 14 Comparison of the weld pool flow on the top surface for the different implementations of the Marangoni convection a) constant surface-tension gradient, b) variable surface-tension gradient

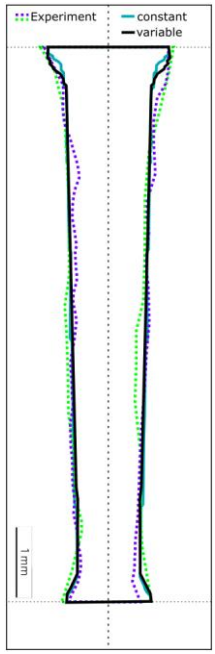

Fig. 15 Comparison of the numerically predicted fusion lines for the constant and variable surface-tension gradient to the experimentally obtained fusion lines

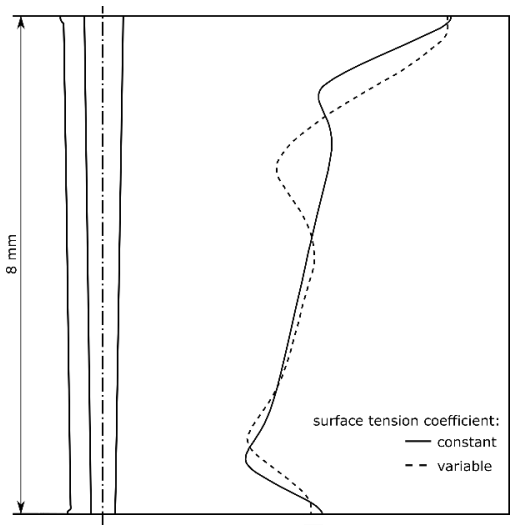

Fig. 16 Comparison of the contours of the calculated weld pool geometries by using the melting isotherms at T_{melt} = 1750 K

TURBULENCE STUDY

To study the influence of a turbulent flow pattern on the weld pool geometry and the fluid flow therein, the results obtained with the three different turbulence models were compared with the results from the laminar model. The corresponding velocity fields to the three studied turbulent formulations and the laminar formulation are shown in Fig. 17; the black lines highlight again the melting isotherms. It is shown that the fusion isotherms at T_{melt} have little to no deviations from each other. However, the velocity fields show minor differences where the maximum velocity for the SST k-ω model is smaller compared to the rest.

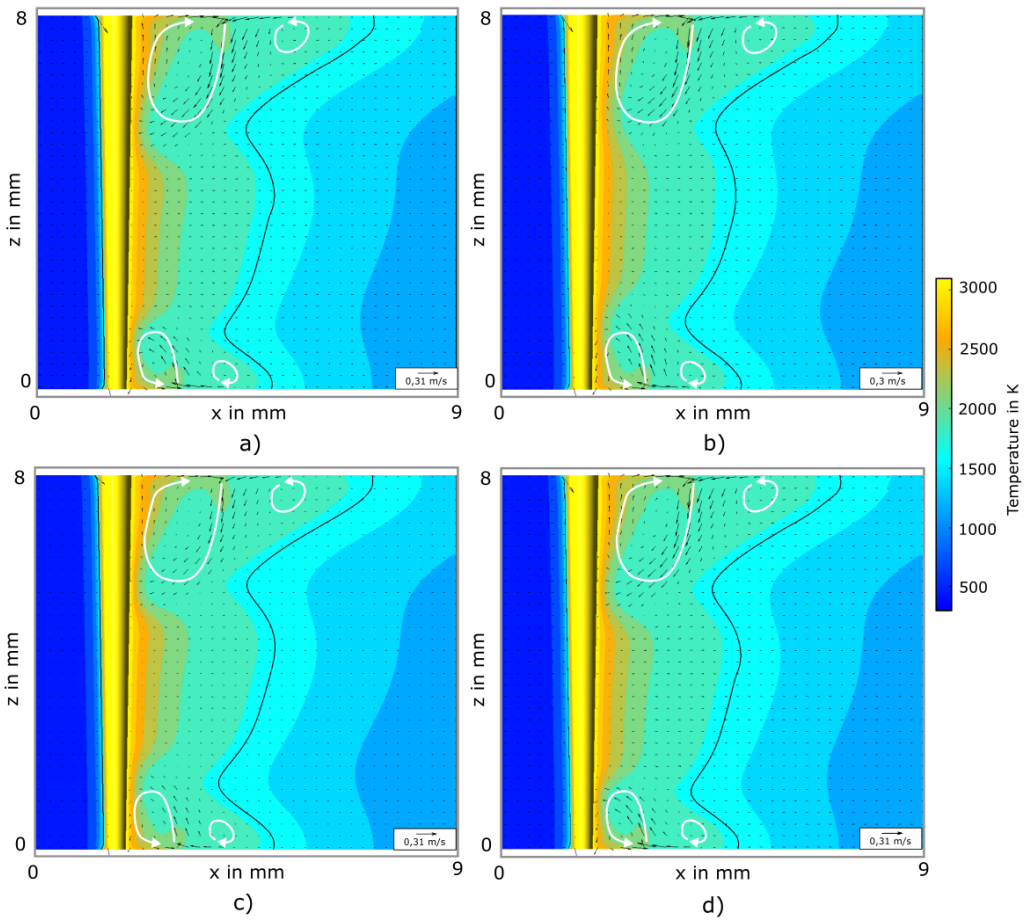

Fig. 17 Calculated velocity fields in the symmetry plane with the different formulations a) laminar formulation, b) SST k-ω model, c) γ transition model, and d) γ-Re_Θ transition model

This observation is confirmed by looking at Fig. 18, which depicts the averaged velocity components within the weld pool, in the x- and y-directions, as well as the average absolute velocity, over the height of the weld pool. The SST γ-Re_{Θ} transition model shows the biggest difference on the upper and lower side of the weld pool compared to the other models, where only small deviations are found. Even though these velocity deviations exist, these seemingly do not affect the weld pool geometry strong enough and barely make up for a small change in the fluid flow and thus in the weld pool shape as well.

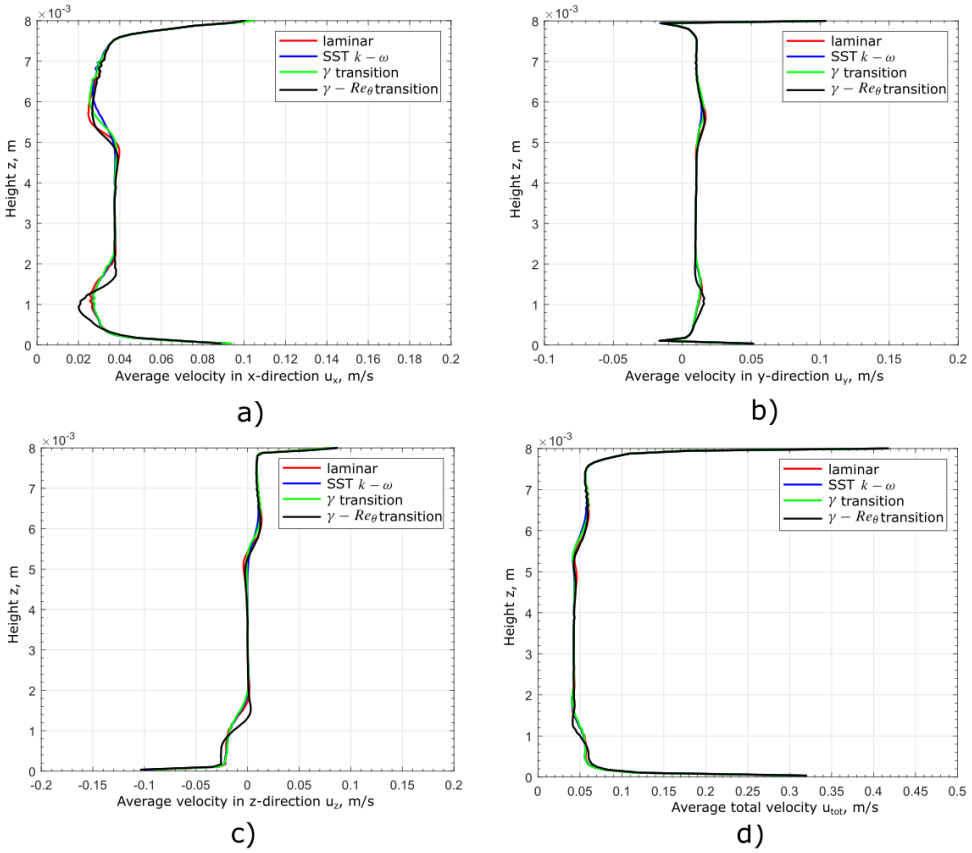

Fig. 18 Computed averaged velocity components in the weld pool with the four studied formulations in a) x-direction, b) y-direction, c) z-direction, and d) the computed averaged total velocity

The numerically predicted fusion lines with the different turbulence models and the laminar model are shown in Fig. 19. It can be concluded that the studied turbulence models resulted in very similar fusion lines. Nonetheless, the fusion line predicted with the laminar formulation slightly differs from the fusion lines obtained with the turbulent models.

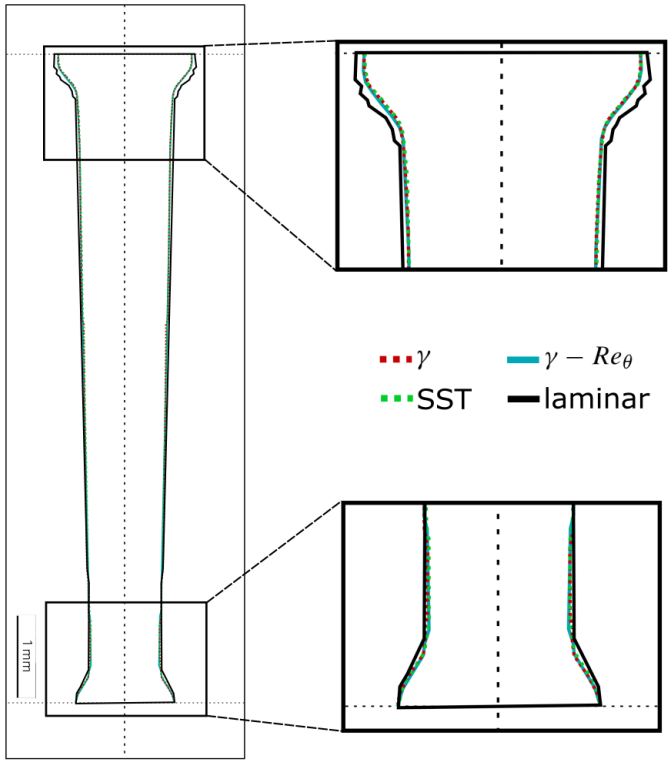

Fig. 19 Comparison of the fusion lines obtained by the laminar formulation and turbulence models

CONCLUSIONS

The present work aimed at extending an existing numerical model to accurately predict the steady-state weld pool shape in complete penetration laser beam welding. To validate the numerical results, experiments were carried out. The measured results were used to validate the laminar formulation of the model by comparing the weld pool length, the fusion lines, and the time-temperature curves. In addition, to assure numerical accuracy, a mesh sensitivity study was performed using a specially designed hybrid mesh. To study the influence of the Marangoni convection on the weld pool geometry, the influence of the surface-active elements was either considered or neglected in the model. Furthermore, a turbulence study was performed to investigate the influence of a turbulent flow pattern on the weld pool geometry and the corresponding velocity fields. The following conclusions were drawn from the obtained numerical and experimental results:

- The experimentally determined fusion lines, time temperature curves and weld pool lengths were used to validate the model and agreed well with the numerically predicted results.

- The mesh sensitivity analysis showed that a minimum element size of $7 \cdot 10^{-5}$ m was necessary to obtain mesh-independent results for the studies performed in the present work.
- The study of the influence of the Marangoni convection on the weld pool geometry showed that sulfur amounts of about 350 ppm may lead to visible changes in the fluid dynamics. As a result, the weld pool shape changes slightly in the regions below and above the top and bottom surface. Nonetheless, no change in the dimensions of the remaining regions, e.g., in the weld pool length on the top and bottom surfaces, was observed.
- According to the turbulence study, the weld pool geometry for the laminar and turbulent formulations practically did not change, however there are minor deviations in the developed fluid flow in the weld pool.
- Based on the obtained results, it can be concluded that the consideration of the surface-active elements and the accounting for turbulence has barely a practical influence on the weld pool geometry when the unalloyed structural steel EH36-N is utilized. Therefore, their consideration is not needed when the main objective of the model is to predict the weld pool geometry.

ACKNOWLEDGEMENTS

This work is funded by the Deutsche Forschungsgemeinschaft (DFG, German Research Foundation) project Nr. 411393804 (BA 5555/5-2), Nr. 416014189 (BA 5555/6-1), and Nr. 466939224 (BA 5555/9-1).

References

[1] M. BACHMANN, A. GUMENYUK, M. RETHMEIER: 'Welding with high-power lasers: trends and developments', *Phys. Proc*., 83 15-25, 2016.

[2] X. ZHANG, E. ASHIDA, S. TARASAWA, Y. ANMA, M. OKADA, S. KATAYAMA, M. MITZUTANI: 'Welding of thick stainless steel plates up to 50 mm with high brightness lasers', *J. Laser Appl.*, 23 (2) 022002, 2011.

[3] J. F. READY, D. F. FARSON (EDS.): 'LIA Handbook of Laser Materials Processing', *Laser Institute of America*, Orlando, 2001.

[4] J. SCHUSTER, S. KEITEL, E. SCHULZE, H. MALY: 'Fachbeiträge-Entstehung erstarrungsbedingter Risse in Laserstrahlschweissverbindungen an unlegierten und niedriglegierten Baustahlen', *Schweißen und Schneiden*, NO. 51, PP. 252-257, 1999.

[5] J. SCHUSTER: 'Heißrisse in Schweißverbindungen: Entstehung, Nachweis und Vermeidung', *DVS-Verlag*; 2004.

[6] M. O. GEBHARDT, A. GUMENYUK, M. RETHMEIER: 'Numerical analysis of hot cracking in laser hybrid welded tubes', *Advances in Materials Science and Engineering*, 520786, 2013.

[7] A. ARTINOV, N. BAKIR, M. BACHMANN, A. GUMENYUK M. RETHMEIER: 'Weld pool shape observation in high power laser beam welding', *Physics Procedia*, 2018.

[8] A. B. D. GINGELL AND T. G. GOOCH: 'Review of factors influencing porosity in aluminium arc welds', *TWI members report*, Ref: 7322.01/97/954.3, 1997.

[9] B. F. DIXON AND J. C. RITTER: 'Solidification cracking in high strength steels welded by electron beam and laser beam processes', *Today and Tomorrow in Science and Technology of*

Welding and Joining, Proceedings 7th International JWS Symposium, Kobe, Japan, November 2001.

[10] T. SHIDA, H. OKUMURA, Y. KAWADA: 'Effects of welding parameters and prevention of defects in deep penetration electron beam welding of heavy section steel plates', *Welding in the World*, pp. 196-207, 1979.

[11] C. ZHANG, M. GAO, D. WANG, J. YIN, X. ZENG: 'Relationship between pool characteristic and weld porosity in laser arc hybrid welding of AA6082 aluminum alloy', *Journal of Materials Processing Technology*, Volume 240, 2017.

[12] S. TSUKAMOTO, H. IRIE, M. INAGAKI: 'Welding Defects and Molten Metal Behaviour in Electron Beam Welding', *The fourth international Symposium of the Japan Welding Society*, pp. 115-120, 1982.

[13] S. TSUKAMOTO, H. IRIE: 'Welding defects and molten metal behaviour in low speed electron beam welding', *Welding in the World*, 23, pp. 130-140, 1985.

[14] S. TSUKAMOTO, H. IRIE: 'Mechanism of locally delayed solidification in electron beam welding', *Welding international*, pp. 177-183, 1991.

[15] A. ARTINOV, M. BACHMANN, X. MENG, V. KARKHIN, M. RETHMEIER: 'On the relationship between the bulge effect and the hot cracking formation during deep penetration laser beam welding', *Procedia CIRP*, Volume 94, 2020.

[16] D. T. SWIFT-HOOK, A. E. F. GICK: 'Penetration welding with lasers', *Welding journal* 52, Nr. 11, pp. 492-499, 1973.

[17] K. N. LANKALAPALLI, J. F. TU, M. GARTNER: 'A model for estimating penetration depth of laser welding processes', *Journal of Physics D: Applied Physics*, 29. Jg., Nr. 7, p. 1831, 1996.

[18] C. CHAN, J. MAZUMDER, M. M. CHEN: 'A two-dimensional transient model for convection in laser melted pool', *Metallurgical Transactions A*, 15. Jg., Nr. 12, pp. 2175-2184, 1984.

[19] Y. F. HSU, B. RUBINSKY: 'Two-dimensional heat transfer study on the keyhole plasma arc welding process', *International Journal of Heat and Mass Transfer*, 31. Jg., Nr. 7, pp. 1409-1421, 1988.

[20] M. BECK: 'Modellierung des Lasertiefschweißens', *Teubner*, 1996.

[21] A. ARTINOV, M. BACHMANN, M. RETHMEIER: 'Equivalent heat source approach in a 3D transient heat transfer simulation of full-penetration high power laser beam welding of thick metal plates', *International Journal of Heat and Mass Transfer*, 122. Jg., pp. 1003-1013, 2018.

[22] M. GEIGER, K. H. LEITZ, H. KOCH, A. OTTO: 'A 3D transient model of keyhole and melt pool dynamics in laser beam welding applied to the joining of zinc coated sheets', *Production Engineering*, 3. Jg., Nr. 2, pp. 127-136, 2009.

[23] D. W. CHO, W. I. CHO, S. J. NA: 'Modeling and simulation of arc: Laser and hybrid welding process', *Journal of Manufacturing Processes*, 16. Jg., Nr. 1, pp. 26-55, 2014.

[24] X. MENG, M. BACHMANN, A. ARTINOV, M. RETHMEIER: 'Experimental and numerical assessment of weld pool behavior and final microstructure in wire feed laser beam welding with electromagnetic stirring', *Journal of Manufacturing Processes*, 45. Jg., pp. 408-418, 2019.

[25] A. ARTINOV, X. MENG, M. BACHMANN, M. RETHMEIER: 'Study on the transition behavior of the bulging effect during deep penetration laser beam welding', *International Journal of Heat and Mass Transfer*, 184. Jg., p. 122171, 2022.

[26] S. PANG, L. CHENG, J. ZHOU, Y. YIN, T. CHEN: 'A three-dimensional sharp interface model for self-consistent keyhole and weld pool dynamics in deep penetration laser welding', *Journal of Physics D: Applied Physics*, 44. Jg., Nr. 2, p. 025301, 2010.

[27] M. BACHMANN: *Numerische Modellierung einer elektromagnetischen Schmelzbadkontrolle beim Laserstrahlschweißen von nicht-ferromagnetischen Werkstoffen*, thesis, Bundesanstalt für Materialforschung und-prüfung (BAM), 2014.

[28] DIN EN 10025-2:2019-10: 'Part 2: Technical delivery conditions for non-alloy structural steels'.
[29] W. TAN, N. S. BAILEY, C. S. YUNG: 'Investigation of keyhole plume and molten pool based on a three-dimensional dynamic model with sharp interface formulation', *Journal of Physics D: Applied Physics*, 46(5) 055501, 2013.
[30] T.E. FABER: 'Fluid Dynamics for Physicists', *Cambridge University Press*, 1995.
[31] A. D. BRENT, V. R. VOLLER, K. T. J. REID: 'Enthalpy-porosity technique for modelling convection-diffusion phase change: application to the melting of a pure metal', *Numerical Heat Transf., Part A Applications*, pp. 297-318, 1988.
[32] ESI GROUP: Material Database, 2009.
[33] F. RICHTER: 'Physikalische Eigenschaften von Stählen und ihre Temperaturabhängigkeit', *Stahleisen-Sonderbericht, Heft* 10, 1983.
[34] J. HILDEBRAND: *Numerische Schweißsimulation-Bestimmung von Temperatur, Gefüge und Eigenspannung an Schweißverbindungen aus Stahl- und Glaswerkstoffen*, thesis, Bauhaus-Universität Weimar, 2008.
[35] P. SAHOO, T. DEBROY, M. J. MCNALLAN: 'Surface tension of binary metal-surface active solute systems under conditions relevant to welding metallurgy', *Metall. Mater. Trans*, pp. 483-491, 1988.
[36] K.C. MILLS: 'Recommended Values of Thermophysical Properties for Selected Commercial Alloys', *Woodhead Publishing*, 2002.
[37] H. HÜGEL, F. DAUSINGER: 'Fundamentals of Laser Induced Processes', *Landolt-Börnstein VIII/1C*, 2004.
[38] P. SHCHEGLOV, S. A. USPENSKIY, A. GUMENYUK, V. N. PETROVSKIY, M. RETHMEIER, V. M. YERMACHENKO: 'Plume attenuation of laser radiation during high power fiber laser welding', *Laser Phys. Lett*., pp. 475-480, 2011.
[39] P. SHCHEGLOV, A. GUMENYUK, I. B. GORNUSHKIN, M. RETHMEIER, V. N. PETROVSKIY: 'Vapor-plasma plume investigation during high-power fiber laser welding', *Laser Phys.*, p. 016001, 2013.
[40] J. GOLDAK, A. CHAKRAVARTI, M. BIBBY: 'A new finite element model for welding heat sources', *Metallurgical transactions B*, pp. 299-305, 1984.
[41] M. COURTOIS, M. CARIN, P. LE MASSON, S. GAIED: 'A two-dimensional axially-symmetric model of keyhole and melt pool dynamics during spot laser welding', *Metallurgical Research & Technology*, 110(2), pp. 165-173, 2013.
[42] S. PANG, X. CHEN, X. SHAO, S. GONG, J. XIAO: 'Dynamics of vapor plume in transient keyhole during laser welding of stainless steel: Local evaporation, plume swing and gas entrapment into porosity', *Optics and Lasers in Engineering*, Volume 82, pp. 28-40, 2016.
[43] X. CHEN, S. PANG, X. SHAO, C. WANG, X. ZHANG, P. JIANG & J. XIAO: 'Sub-microsecond vapor plume dynamics under different keyhole penetration regimes in deep penetration laser welding', *Journal of Physics D: Applied Physics*, 50(20), 2017.
[44] V. R. VOLLER, C. PRAKASH: 'A fixed grid numerical modelling methodology for convection-diffusion mushy region phase-change problems', *International journal of heat and mass transfer*, pp. 1709-1719, 1987.
[45] V. BRUYERE, C. TOUVREY, P. Namy: 'A phase field approach to model laser power control in spot laser welding', *Proceedings of the 2014 Comsol Conference*, Cambridge, 2014.
[46] ANSYS FLUENT: 'ANSYS fluent theory guide', *ANSYS Inc*., USA, 2021.
[47] K. C. MILLS, E. D. HONDROS, M. MCLEAN: 'Marangoni effects in welding', *Philosophical Transactions of the Royal Society of London. Series A: Mathematical, Physical and Engineering Sciences*, Nr. 1739, pp. 911-925, 1998.
[48] A. FEY, S. ULRICH, S. JAHN, P. SCHAAF: 'Numerical analysis of temperature distribution during laser deep welding of duplex stainless steel using a two-beam method', *Welding in the World*, Nr. 4, pp. 623-632, 2020.

[49] R. T. C. CHOO, J. SZEKELY: 'The possible role of turbulence in GTA weld pool behavior', *Welding Journal-New York*, p. 25, 1994.
[50] W. RODI, G. SCHEUERER: 'Scrutinizing the k-ε turbulence model under adverse pressure gradient conditions', *J. Fluids Eng.*, pp. 174-179, 1986.
[51] ISO/TS 18166:2016 'Numerical welding simulation Execution and documentation'.